

TMDC-based topological nanospaser: single and double threshold behavior

Rupesh Ghimire,^{*} Jhih-Sheng Wu,[†] Fatemeh Nematollahi,[‡] Vadym Apalkov,[§] and Mark I. Stockman[¶]
Center for Nano-Optics (CeNO) and Department of Physics and Astronomy,
Georgia State University, Atlanta, Georgia 30303

(Dated: January 19, 2021)

We theoretically study a topological nanospaser, which consists of a silver nanospheroid and MoS₂ monolayer flake of a circular shape. The metal nanospheroid acts as a plasmonic nanoresonator that supports two rotating modes, which are coupled to the corresponding valleys of MoS₂. We apply external circularly polarized light that selectively pumps only one of the valleys of MoS₂. The generated spaser dynamics strongly depends on the size (radius) of the MoS₂ nanoflake. For small radius, the system has only one spasing regime when only chirally-matched plasmon mode is generated, while at larger size of MoS₂, depending on the pump intensity, there are two regimes. In one regime, only the chirally-matched plasmon mode is generated, while in the other regime both chirally-matched and chirally-mismatched modes exist. Different regimes of spaser operation have also opposite handedness of the far-field radiated of the spaser system. Such topological nanospaser has potential applications in different areas of infrared spectroscopy, sensing, probing, and biomedical treatment.

I. INTRODUCTION

The advent of spaser (surface plasmon amplification by stimulated emission of radiation) stems from a work published in 2003 [3], an idea, which initiated a distinct new approach for generation and amplification of nanolocalized fields. Spaser itself has seen tremendous development due to its boundless possibilities. Such metal resonator system allows one to scale down the spatial size of a laser and, at the same time, to satisfy all the ingredients of a perfect lasing system, i.e., optical confinement, feedback, and thermal management. After the first experimental observation of a spaser [29, 30], many theoretical developments have set in to the scene [2, 12, 20, 36, 50], which ushered to plethora of new designs and applications. The operational frequencies of spasers cover a wide range of spectrum from infrared to near-ultraviolet and this is one of the key factors of its rapid emergence in the optical research [7, 13, 19, 22, 25, 26, 38, 39, 49].

Spaser, apart from fundamental research, has proved itself viable for different potential applications as an element of opto-electronic systems [8–10, 18, 28, 33–35], as a sensor of chemical and biological agents [6, 41, 42, 52], and as a biological probe [11, 14] for therapeutics and diagnostics of different diseases, e.g., cancer.

The first experimentally realized spaser is a nanoshell spaser[29]. It consists of a metal nanocore surrounded by a dielectric gain medium. The metal core supports the plasmonic modes, which optically interact with the gain medium. The gain medium usually consists of dye molecules [14, 29], however, different materials such as perovskites and 2D systems can be used as a gain

element[27, 44]. The size of such spaser can be as small as tens of nanometers.

The other type of spaser that consists of a nanorod (gain medium) placed near a plasmonic metal has been proposed in Ref. [30]. Such spaser is generally a micrometer in size and can be used as a good source of the far-field radiation. The operation of such plasmonic nanolasers is based on the same principles as the ones of the nanoshell spaser but with one key difference. Namely, their plasmonic modes are not the localized modes as in the case of the nanoshell spaser but the propagating modes, which are called the surface plasmon polaritons (SSPs) [23–25, 40, 47, 49].

A spaser design, which is based on a periodic array of nano-resonators that have coherent extended collective modes, has been proposed in Ref.[16, 31, 50]. Such spaser consists of either an array of nanocavities embedded in a metal film [39] or a periodic set of metal nanoparticles suspended in a gain medium [51]. For a special arrangement of metal nanoparticles, the system has topologically nontrivial collective plasmonic excitations. The corresponding spaser, which is called a topological spaser of type I, has been proposed in Ref. [45]. In such spaser, two types of metal nanoshells form the honeycomb crystal structure with the broken inversion symmetry. The collective plasmonic excitations of such system have two types of topologically nontrivial chiral modes with opposite chiralities, i.e., opposite topological charges. The modes are located at the K and K' valleys in the corresponding reciprocal space[45]. In such topological spaser, the nontrivial topology is introduced into the plasmonic excitations of the system.

There is also another type of topological spaser, called the topological spaser of type II[15], in which the plasmonic system is topologically trivial but the gain medium has nontrivial topology. The example of such gain medium is a nanopatch of a transition-metal dichalcogenide (TMDC) monolayer. In the reciprocal space, TMDC monolayer has two valleys, K and K' , which have

^{*} rghimire1@student.gsu.edu

[†] b91202047@gmail.com

[‡] fnematollahi1@gsu.edu

[§] vapalkov@gsu.edu

[¶] mstockman@gsu.edu

chiral electron states and are characterized by nonzero and opposite topological charges. Plasmonic modes in such nanopaser are generated in a metal nanoparticle that is placed atop of TMDC nanopatch. Thus the topology in the system is introduced only through the gain medium. We have shown in Ref. [15] that the plasmonic modes of such nanopaser are topologically protected and determined by the topological charge of the excited valley of TMDC nanopatch. The topological spaser of type II has been studied in Ref. [15] for small size of TMDC nanopatch, which is comparable to the size of the metal nanoparticle. In the present paper we extend this theoretical analysis to large sizes of TMDC monolayer and show that the topological nanopaser under this condition has very rich dynamics with different types of plasmonic modes that are generated.

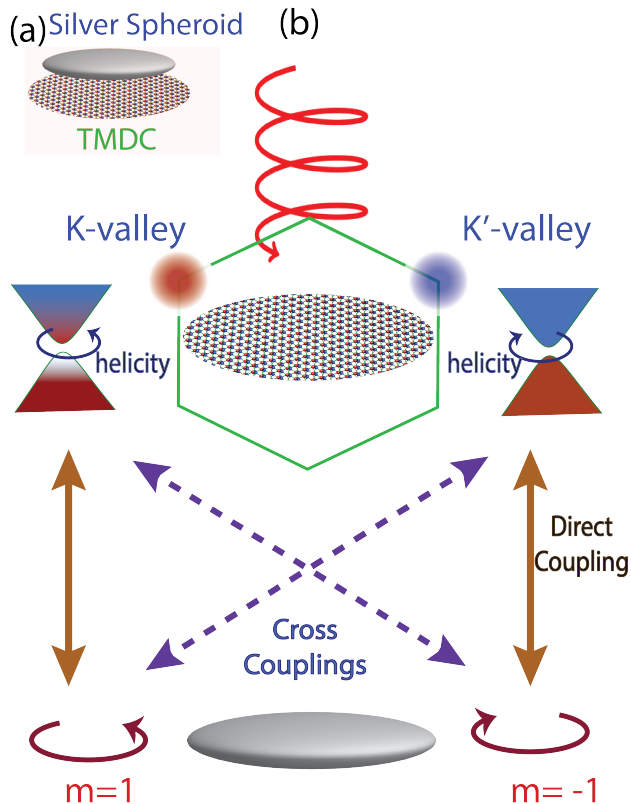


FIG. 1. Schematics of the topological spaser. (a) Spaser consists of a silver nanospheroid placed on the top of TMDC nanoflake of a circular shape. The silver nanospheroid has oblate shape with radius 12 nm and height 1.2 nm. (b) Schematic of spaser operation. A circular-polarized light excites the valley with the chirality that match the light helicity. The metal nanospheroid supports two plasmon modes with azimuthal quantum numbers $m = -1$ and $m = 1$. The stimulated CB \rightarrow VB transitions at the corresponding K or K' points couple to these plasmon modes through direct and cross couplings.

II. MODEL AND MAIN EQUATIONS

The topological nanopaser of type II consists of a metal nanospheroid placed on the top of a TMDC nanopatch - see Fig. 1(a). We assume that the nanospheroid has an oblate shape with the radius of 12 nm and the height of 1.2 nm. The TMDC nanopatch has a circular shape with the radius that is considered as a parameter below. The whole system is placed in dielectric medium with dielectric constant $\epsilon = 2$.

The TMDC monolayer has two valleys, K and K' , which have opposite topological charges (chiralities). When TMDC monolayer is illuminated with circularly polarized light, only one of the valleys with the chirality that corresponds to the handedness of the circularly polarized light is excited [5, 48]. For concreteness, we assume that circularly polarized light excites only the K valley [see Fig. 1(b)]. We characterize such continuous excitation by the corresponding rate $g\kappa$.

The metal nanospheroid has azimuthal symmetry and the corresponding plasmonic modes are characterized by azimuthal quantum number m . Because of the chiral nature of TMDC valleys, the K valley is predominantly coupled to the $m = 1$ plasmon mode, while the K' valley is mainly coupled to the $m = -1$ mode of the nanospheroid. In Fig. 1(b), these couplings are marked as the direct couplings. The selection rules corresponding to the direct couplings are exact at the center of TMDC nanopatch ($\vec{r} = 0$) and approximate at any other points within TMDC. As a result there are also cross couplings of the plasmonic modes and TMDC valleys, which are shown schematically in Fig. 1(b).

Thus in the topological nanopaser of type II, the circularly polarized light excites one of the valleys (say K) of TMDC monolayer (gain medium), which then excites the $m = 1$ plasmonic mode through the direct coupling. Such mode is also coupled to the other valley (K') through the cross coupling and excites electrons in the K' valley, which finally excites the $m = -1$ plasmonic mode through the direct coupling. Thus all modes of the system are coupled and the final kinetics of the system strongly depends on its parameters, e.g., the radius of TMDC nanopatch, which controls the magnitudes of both direct and cross couplings.

Within the quasistatic approximation, the plasmonic eigenmodes of nanospheroid, $\phi_m(\mathbf{r})$, satisfy the following equation[37]

$$\frac{\partial}{\partial \mathbf{r}} \theta(\mathbf{r}) \frac{\partial}{\partial \mathbf{r}} \varphi_n(\mathbf{r}) - s_n \frac{\partial^2}{\partial \mathbf{r}^2} \varphi_n(\mathbf{r}) = 0, \quad (1)$$

$$s_n = \frac{\int_{\text{All Space}} \theta(\mathbf{r}) |\nabla \phi_m(\mathbf{r})|^2 d^3 \mathbf{r}}{\int_{\text{All Space}} |\nabla \phi_m(\mathbf{r})|^2 d^3 \mathbf{r}}, \quad (2)$$

where s_n is the eigenvalue of the n th mode, θ is a characteristic function which is 1 inside and 0 outside the metal. For the oblate nanospheroid, which has azimuthal symme-

try, the eigenmodes are characterized by two spheroidal quantum numbers[43]: multipolarity $l = 1, 2, \dots$ and azimuthal or magnetic quantum number $m = 0, \pm 1, \dots$. In our case the relevant modes are the dipole modes with $l = 1$ and $m = \pm 1$.

The Hamiltonian of our system has the following form

$$H = H_{SP} + H_{gain} + H_{int}, \quad (3)$$

where H_{SP} is the Hamiltonian of surface plasmons (SP) (nanospheroid), H_{gain} is the Hamiltonian of TMDC nanopatch (gain medium), and H_{int} describes the interaction between the plasmonic system and the gain medium.

The Hamiltonian of SP, H_{SP} , in the quantum mechanical description, is given by the following expression

$$H_{SP} = \hbar\omega_{sp} \sum_{m=\pm 1} \hat{a}_m^* \hat{a}_m, \quad (4)$$

where ω_{sp} is the SP frequency, \hat{a}_m^\dagger and \hat{a}_m are creation and annihilation operators of the corresponding plasmon with quantum number $m = \pm 1$. Then the electric field operator is [3, 36]

$$\mathbf{F}_m(\mathbf{r}, t) = - \sum_{m=1, -1} A_{sp} (\nabla \phi_m(\mathbf{r}) \hat{a}_m e^{-i\omega t} + \nabla \phi_m^*(\mathbf{r}) \hat{a}_m^* e^{i\omega t}), \quad (5)$$

$$A_{sp} = \sqrt{\frac{4\pi\hbar s_n}{\epsilon_d s'_n}} \quad \text{and} \quad s'_n \equiv \left. \frac{d\text{Re}[s(\omega)]}{d\omega} \right|_{\omega=\omega_{sp}}. \quad (6)$$

The electric field depends on the position within TMDC monolayer through the position dependent plasmonic mode, $\phi_m(\mathbf{r})$. The interaction Hamiltonian describes the dipole coupling of the plasmonic excitations and the electron system in TMDC monolayer and is given by the following expression

$$H_{int} = -\nu_{\mathcal{K}} \sum_{\mathcal{K}=\mathbf{K}, \mathbf{K}'} \int d^2\mathbf{r} \sum_{m=\pm 1} \mathbf{F}_m(\mathbf{r}) \hat{\mathbf{d}}_{\mathcal{K}}(\mathbf{r}), \quad (7)$$

where \mathcal{K} is the valley index, \mathbf{K} or \mathbf{K}' , $\nu_{\mathcal{K}}$ is the density of electron states at the \mathcal{K} valley, which can be found from the experimental data[32, 46]: $\nu_{\mathcal{K}} = 7.0 \times 10^{12} \text{ cm}^{-2}$. Here the interband dipole matrix element, $\mathbf{d}_{\mathcal{K}}$, between the VB and CB states of TMDC, is proportional to the non-Abelian Berry connection

$$\mathbf{d}_{\mathcal{K}} = e\mathcal{A}^{(cv)}(\mathbf{k}), \quad \mathcal{A}^{(cv)}(\mathbf{k}) = i \left\langle u_{c\mathbf{k}} \left| \frac{\partial}{\partial \mathbf{k}} \right| u_{v\mathbf{k}} \right\rangle \Bigg|_{\mathbf{k}=\mathcal{K}}, \quad (8)$$

where $u_{c\mathbf{k}}$ and $u_{v\mathbf{k}}$ are the lattice Bloch functions.

The optical transitions in TMDC nanopatch, which are the transitions between the valence band (VB) and the conduction band (CB), are characterized by the transition frequency ω_{21} , which is the same for both \mathbf{K} and \mathbf{K}' valleys due to time reversal symmetry of the system. Below we choose the parameters of nanospheroid for which

the SP frequency ω_{sp} is equal to the transition frequency ω_{21} .

The spaser dynamics is described within the semiclassical approach. Within this approach the plasmonic system is treated classically, i.e., the creation and annihilation operators ($\hat{a}_m = a_m$ and $\hat{a}_m^\dagger = a_m^*$) are considered as complex numbers, and, at the same time, the electron system in TMDC (gain medium) is described quantum mechanically using the density matrix $\hat{\rho}_{\mathcal{K}}(\mathbf{r}, t)$. In the rotating wave approximation (RWA) [1, 4] the density matrix has the following form

$$\hat{\rho}_{\mathcal{K}}(\mathbf{r}, t) = \begin{pmatrix} \rho_{\mathcal{K}}^{(c)}(\mathbf{r}, t) & \rho_{\mathcal{K}}(\mathbf{r}, t) e^{i\omega t} \\ \rho_{\mathcal{K}}^*(\mathbf{r}, t) e^{-i\omega t} & \rho_{\mathcal{K}}^{(v)}(\mathbf{r}, t) \end{pmatrix}. \quad (9)$$

Then the corresponding semiclassical equations can be derived from Hamiltonian (3),

$$\dot{a}_m = [i(\omega - \omega_{sp}) - \gamma_{sp}] a_m + i\nu_{\mathcal{K}} \int_S d^2\mathbf{r} \sum_{\mathcal{K}} \rho_{\mathcal{K}}^*(\mathbf{r}) \tilde{\Omega}_{m, \mathcal{K}}^*(\mathbf{r}), \quad (10)$$

$$\dot{n}_{\mathcal{K}}(\mathbf{r}) = -4 \sum_{m=1, -1} \text{Im} \left[\rho_{\mathcal{K}}(\mathbf{r}) \tilde{\Omega}_{m, \mathcal{K}}^*(\mathbf{r}) a_m \right] + g_{\mathcal{K}} [1 - n_{\mathcal{K}}(\mathbf{r})] - \gamma_{2\mathcal{K}}(\mathbf{r}) [1 + n_{\mathcal{K}}(\mathbf{r})], \quad (11)$$

$$\dot{\rho}_{\mathcal{K}}(\mathbf{r}) = [-i(\omega - \omega_{21}) - \Gamma_{12}] \rho_{\mathcal{K}}(\mathbf{r}) + i n_{\mathcal{K}}(\mathbf{r}) \sum_{m=1, -1} \tilde{\Omega}_{m, \mathcal{K}}^* a_m^*, \quad (12)$$

where S is the area of TMDC nanoflake, Γ_{12} is the polarization relaxation rate, $g_{\mathcal{K}}$ is the pumping rate of the \mathcal{K} valley, and $\tilde{\Omega}_{m, \mathcal{K}}(\mathbf{r})$ is the Rabi frequency,

$$\tilde{\Omega}_{m, \mathcal{K}}(\mathbf{r}) = -\frac{1}{\hbar} A_{sp} \nabla \phi_m(\mathbf{r}) \mathbf{d}_{\mathcal{K}}. \quad (13)$$

Here the population inversion, $n_{\mathcal{K}}$, is defined as

$$n_{\mathcal{K}} \equiv \rho_{\mathcal{K}}^{(c)} - \rho_{\mathcal{K}}^{(v)}, \quad (14)$$

and the spontaneous emission rate, $\gamma_{2\mathcal{K}}(\mathbf{r})$, of the SPs is [36]

$$\gamma_{2\mathcal{K}}(\mathbf{r}) = \frac{2(\gamma_{sp} + \Gamma_{12})}{(\omega_{sp} - \omega_{21})^2 + (\gamma_{sp} + \Gamma_{12})^2} \sum_{m=1, -1} \left| \tilde{\Omega}_{m, \mathcal{K}}(\mathbf{r}) \right|^2 \quad (15)$$

III. RESULTS AND DISCUSSIONS

A. Parameters of topological spaser

The system consists of three components: a silver nanospheroid, a TMDC monolayer nanoflake, and a surrounding dielectric medium. A silver nanospheroid has

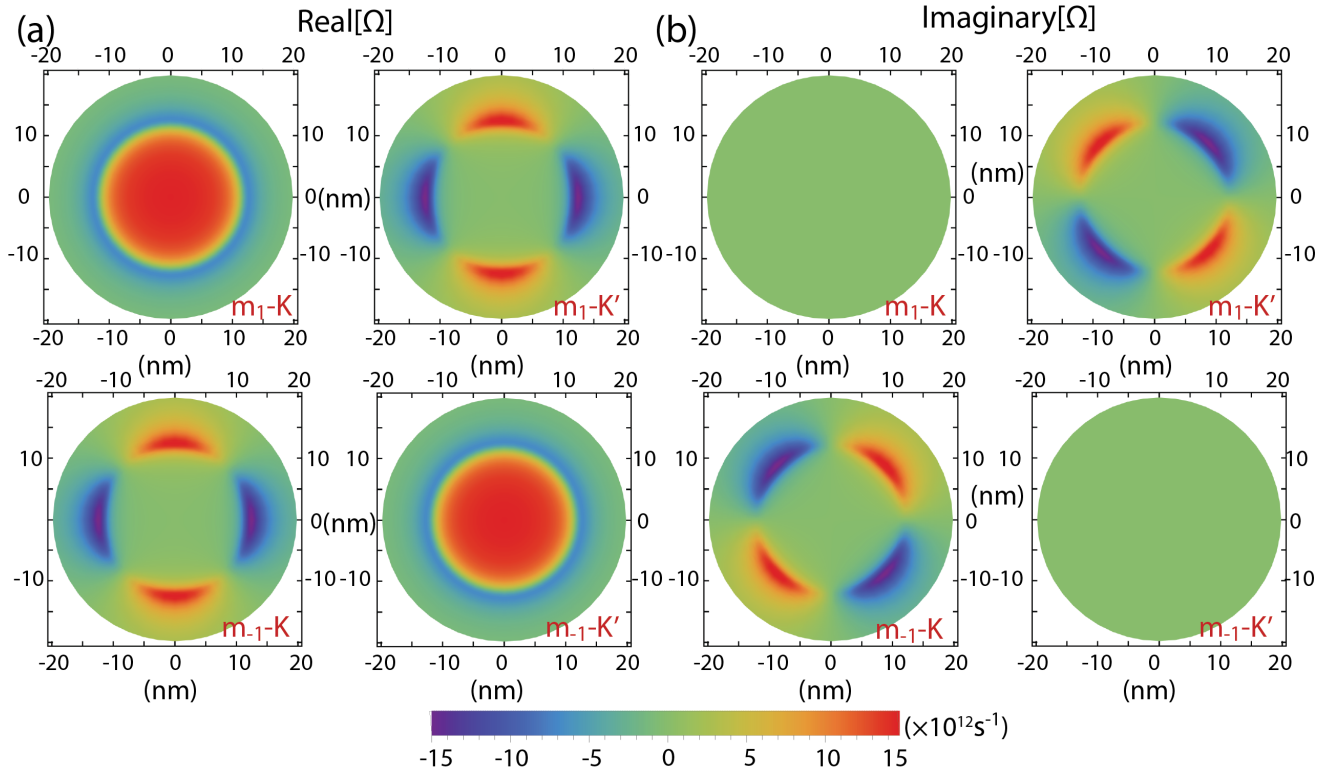


FIG. 2. The real part (a) and imaginary part (b) of the Rabi frequency. The Rabi frequency determines the coupling of the plasmon mode m and the K or K' valleys of TMDC. The radius of the metal spheroid is $a = 12$ nm.

an oblate shape with the radius of 12 nm and the height of 1.2 nm. These are the semi-major (a) and semi-minor (c) axes of an oblate system. We choose a MoS₂ monolayer as a TMDC material. The MoS₂ nanoflake has a circular shape and is placed on the top of the nanospheroid. Below we change the radius of MoS₂ nanoflake. Both the nanospheroid and MoS₂ monolayer are suspended in dielectric medium with the permittivity of $\epsilon_d = 2$.

The height of nanospheroid, c , is chosen in a such way that the SP frequency ω_{sp} matches the dipole transition frequency $\omega_{21} = \Delta_g/\hbar$ of MoS₂. Here Δ_g is the bandgap of MoS₂ monolayer. The band structure of MoS₂ was calculated within the three-band tight binding model[21]. From this model we obtained both the bandgap and the dipole matrix elements between the conduction and valence bands at the K and K' points: $\Delta_g = 1.66$ eV; $\mathbf{d}_{\mathbf{K}} = 17.7 \mathbf{e}_+$ D, and $\mathbf{d}_{\mathbf{K}'} = 17.7 \mathbf{e}_-$ D, where $\mathbf{e}_{\pm} = (\mathbf{e}_x \pm i\mathbf{e}_y)/\sqrt{2}$ are the chiral unit vectors.

The other parameters, which have been used in our calculations, are the coherent relaxaton rate $\Gamma_{12} = 15.1 \text{ ps}^{-1}$ for MoS₂ monolayer and the plasmon relaxation rate for silver nanoparticle, $\gamma_{sp} = 13.4 \text{ ps}^{-1}$. We also assume that only the K valley is pumped by external circularly polarized light, i.e., $g_{\mathbf{K}} = g$ and $g_{\mathbf{K}'} = 0$. With the above parameters, from the nonlinear system of Eqs. (10)-(49), we obtain both the stationary solution and the kinetics of topological spaser for given initial conditions.

B. The dynamics of topological spaser

We solve the system of Eqs. (10)-(49) numerically with the given initial conditions, which are $N_{m=1} = |a_1|^2 = 9$ ($a_1 = 3$), i.e., there are nine $m = 1$ plasmons, and the conduction band populations of both K and K' valley are zero. We obtain the spaser dynamics for different values of the gain, g , and different radii of TMDC nanoflakes. Here we assume that only one valley, i.e., the K valley, is pumped by the circularly polarized light.

The dynamics of the spaser is completely determined by the coupling of plasmonic excitations and the TMDC system. Such coupling is characterized by the Rabi frequency, $\tilde{\Omega}_{m,\mathcal{K}}(\mathbf{r})$, which is a function of the radius vector, \mathbf{r} , within TMDC nanoflake and also depends on the type of the plasmon, $m = 1$ or $m = -1$, and the valley of TMDC, K or K' . The real and imaginary parts of $\tilde{\Omega}_{m,\mathcal{K}}(\mathbf{r})$ are shown in Fig. 2 for different combinations of m and TMDC valley. The radius of metal nanospheroid, which is 12 nm in the x - y plane, determines two different dependences of $\tilde{\Omega}_{m,\mathcal{K}}(\mathbf{r})$. If $r < 12$ nm, then the Rabi frequency, both the real and imaginary parts, is isotropic function of radius. It mainly follows the "angular momentum" selection rule, i.e., $m = 1$ is coupled to the K valley, while $m = -1$ is coupled to the K' valley. This selection is exact at $r = 0$, but for $r > 0$ it is a good approximation.

For $r > 12$ nm, i.e., a point is outside the metal nanospheroid in the x - y plane, the plasmonic electric field has a dipole nature. As a result, $\tilde{\Omega}_{m,\mathcal{K}}(\mathbf{r})$ behaves completely differently. Namely, both $\tilde{\Omega}_{m=1,K'}$ and $\tilde{\Omega}_{m=-1,K}$ are large, while $\tilde{\Omega}_{m=-1,K'}$ and $\tilde{\Omega}_{m=1,K}$ are small. Also, because of the dipole nature of the plasmonic electric field, the Rabi frequency acquires strong angular dependence of type $\exp(2i\varphi)$ - see Fig. 2, where φ is the polar in-plane angle.

Thus, from the properties of the Rabi frequency, we can conclude that if the radius of TMDC nanoflake is less than 12 nm, then $m = 1$ plasmon mode is mainly coupled to the TMDC valley of the same chirality, i.e., the K valley, while $m = -1$ plasmon mode - to the K' valley. But if the radius of TMDC is greater than 12 nm, then $m = 1$ and $m = -1$ plasmon modes are coupled to both K and K' valleys. The larger the radius of the TMDC flake, the stronger the coupling of the plasmonic mode to the TMDC valley of opposite chirality.

The number of plasmons, $N_m = |a_m|^2$, as a function gain, g , is shown in Fig. 3 (a)-(c) for three different radii of TMDC nanoflake. The solid and dashed lines correspond to $m = 1$ and $m = -1$ plasmons, respectively. If $r = 12$ nm then only co-rotating ($m = 1$) plasmon mode, i.e., the mode that is strongly coupled to the excited K valley, is generated. There is a characteristic spaser threshold, $g_{th} \approx 20$ ps^{-1} , when the plasmon mode starts generating.

For a larger radius, $r = 16$ nm, see Fig. 3(b), the system show different behavior. Now, the K valley is coupled to both co-rotating $m = 1$ and counter-rotating $m = -1$ modes (although the coupling to the counter-rotating mode is still relatively weak). There are two thresholds, $g_{th,1}$ and $g_{th,2}$. At lower threshold, $g_{th,1} \approx 49$ ps^{-1} , only one mode, $m = 1$, is generated, while at larger threshold, $g_{th,2} \approx 70$ ps^{-1} , both plasmon modes, $m = 1$ and $m = -1$, cogenerated. At the second threshold the energy is transferred from the $m = 1$ mode to $m = -1$ mode so the number of $m = 1$ plasmons decreases. Another unique feature of the second regime, $g > g_{tr,2}$, is that there are more counter-rotating plasmons than the co-rotating ones, $N_{-1} > N_1$.

When the radius of the TMDC nanoflake increases even more, $r = 18$ nm, two thresholds, $g_{th,1}$ and $g_{th,2}$, merge into a single one, $g_{th,1} = g_{th,2} \approx 52$ ps^{-1} , at which two plasmon modes are generated simultaneously - see Fig. 3(c). Similar to a smaller radius, the number of counter-rotating plasmons is more than the number of co-rotating ones.

The dependence of two thresholds, $g_{th,1}$ and $g_{th,2}$, on the TMDC radius, r , is shown in Fig. 3(d). At $r \lesssim 15$ nm, there is only one spaser regime when only co-rotating mode is generated. At $15nm \lesssim r \lesssim 17nm$ there are two thresholds and the system can generate either one plasmon mode, $m = 1$, or two plasmons modes, $m = 1$ and $m = -1$, depending on the gain, g . At $r > 17$ nm, two thresholds merge into a single one and there is only one regime with two generated plasmon modes.

To illustrate different regimes of spaser dynamics, we show in Fig. 4 the distributions of the population inversions at the K and K' valleys for the radius of TMDC flake of 16 nm and different values of gain. If the gain is less than the first threshold, $g < g_{th,1}$, then no plasmons are generated and the population inversion of the K valley is close to one, while the population inversion of the K' valley is exactly -1, i.e., the valence band is completely occupied and the conduction band is empty. This case is shown in Fig. 4(a)-(b).

In Fig. 4(c)-(d) the gain is greater than $g_{th,1}$ but less than $g_{th,2}$. In this case only one plasmon mode, $m = 1$, is generated. The distribution of population inversion is isotropic and it is close to zero for $r < 12$ nm for the K valley and for $r > 12$ nm for the K' valley, which illustrates strong coupling of these spatial regions to the $m = 1$ mode -see also Fig. 2.

Another possibility, when the gain is greater than $g_{th,2}$, is shown in Fig. 4(e)-(f). Under this condition, both $m = 1$ and $m = -1$ plasmon modes are generated. They are coupled to both valleys at all spatial regions ($r < 12$ nm and $r > 12$ nm), as a result, the population inversions for both K and K' valleys are close to zero. Because of coexistence of two plasmon modes, the resulting electric field show interference features and the corresponding population inversion distribution is anisotropic - see Fig. 4(c)-(d).

The large radius of TMDC nanoflake, $r = 18$ nm, is illustrated in Fig. 5. In this case there is only one threshold. If the gain is less than the threshold, see Fig. 5(a)-(b), then no plasmons are generated and the conduction band of the K valley is highly populated, while the population inversion of the K' valley is -1 at all spatial points. If the gain is greater than the threshold, see Fig. 5(c)-(d), then two plasmon modes, $m = -1$ and $m = 1$, are generated. The population inversion is close to zero for both K and K' valleys. The population inversion distribution is also anisotropic, which is due to interference of the plasmonic fields of two modes.

The temporal dynamics of the topological spaser is shown in Fig. 6. The initial number of plasmons is nine for both modes, $m = 1$ and $m = -1$. In Fig. 6(a), the gain is fixed, $g = 82$ ps^{-1} , and the results are shown for different radii of TMDC nanoflake. For all parameters, the number of plasmons, N_1 and N_{-1} , show similar initial dynamics (at $t \lesssim 0.15$ ps). Namely, first, both N_1 and N_{-1} sharply decrease to almost zero values, then show small oscillations and finally monotonically increase to the stationary values. At the stationary stage, for small radius of TMDC nanoflake, $r = 14$ nm, only $m = 1$ is generated, while for large radius, $r = 16$ nm or $r = 18$ nm, both modes, $m = 1$ and $m = -1$, are generated - see Fig. 6(a).

This property is also illustrated in Fig. 6(b), in which the radius is fixed, $r = 16$ nm, and the gain is varied. For $g = 50$ ps^{-1} and $g = 60$ ps^{-1} , which are less than the second threshold, only $m = 1$ plasmons are generated in the stationary regime. For large gain, $g = 70$ ps^{-1} , mode

$m = -1$ coexists with $m = 1$ plasmonic mode.

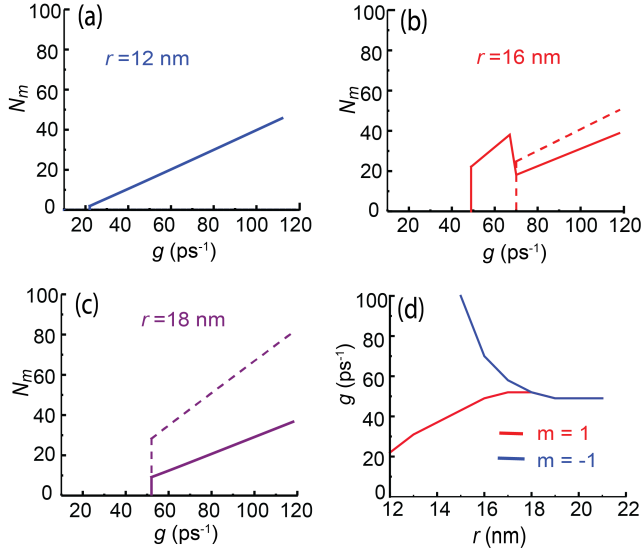


FIG. 3. (a)-(c) Number of plasmons, N_m , as a function of gain, g . The solid and dashed lines correspond to the plasmons with $m = 1$ and $m = -1$, respectively. The radius of TMDC nanoflake is (a) 12 nm, (b) 16 nm, and (c) 18 nm. (d) The topological spaser thresholds as a function of radius of TMDC nanoflake. If $g_{th,2} > g > g_{th,1}$ then only $m = 1$ plasmon mode exists in the stationary regime, while if $g > g_{th,2}$ then both modes $m = 1$ and $m = -1$ are generated.

C. Far-Field Radiation

Although it is not its primary role, the topological nanolaser can be used as a miniature source of far-field radiation, which is due to the oscillating electric dipole of the spaser system. The induced electric dipole moment of the system is the sum of two contributions: the dipole moment of TMDC nanoflake, \mathbf{d}_{tmdc} , and the dipole moment of the metal nanospheroid, $\mathbf{d}_{\text{metal}}$,

$$\mathbf{d}_{\text{total}} = \mathbf{d}_{\text{tmdc}} + \mathbf{d}_{\text{metal}}. \quad (16)$$

The dipole moment of TMDC nanoflake can be expressed in terms of the non-diagonal part of the density matrix of TMDC system

$$\begin{aligned} \mathbf{d}_{\text{tmdc}} &= \sum_{\mathbf{K}=\mathbf{K},\mathbf{K}'} (\rho_{\mathbf{K}} \mathbf{d}_{\mathbf{K}} e^{i\omega t} + \rho_{\mathbf{K}}^* \mathbf{d}_{\mathbf{K}}^* e^{-i\omega t}) \\ &= (\rho_{\mathbf{K}} \mathbf{d}_{\mathbf{K}} + \rho_{\mathbf{K}'} \mathbf{d}_{\mathbf{K}'}) e^{i\omega t} + (\rho_{\mathbf{K}}^* \mathbf{d}_{\mathbf{K}}^* \\ &\quad + \rho_{\mathbf{K}'}^* \mathbf{d}_{\mathbf{K}'}^*) e^{-i\omega t}. \end{aligned} \quad (17)$$

The dipole moment of the metal nanospheroid can be found from the known electric field [see Eq. (5)] inside the metal,

$$\mathbf{d}_{\text{metal}} = \int_V \frac{\text{Re}[\epsilon_{\text{metal}} - \epsilon_d]}{4\pi} \mathbf{F}_{\mathbf{m}}(\mathbf{r}, \mathbf{t}) \, \mathbf{dr}. \quad (18)$$

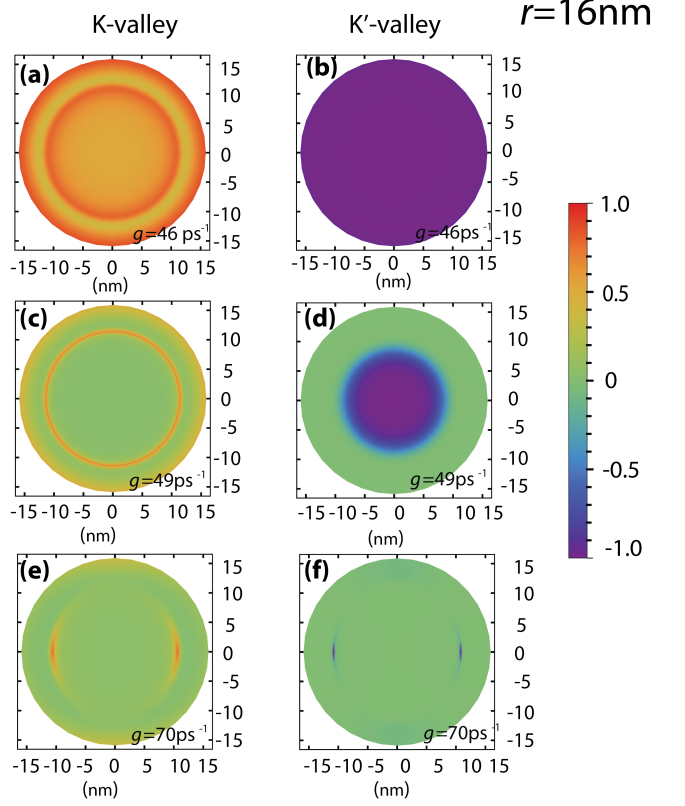


FIG. 4. Inversion population of K and K' valleys of MoS_2 nanoflake with the radius of 16 nm. The gain is (a),(b) 46 ps^{-1} , (c),(d) 49 ps^{-1} , and (e),(f) 70 ps^{-1} . The panels (a), (c), and (e) correspond to the K valley, while the panels (b), (d), and (f) describe the K' valley.

Here the integral is calculated over the volume of the nanospheroid. The electric field, $\mathbf{F}_{\mathbf{m}}(\mathbf{r}, \mathbf{t})$, inside the metal depends on the number of $m = 1$ and $m = -1$ plasmons.

The x and y components of the total dipole moment, which is the sum of Eqs. (48) and (43), can be expressed in the following forms

$$\mathbf{d}_{\text{total},x} = B_1 e^{i\omega t} + \tilde{B}_1 e^{-i\omega t}, \quad (19)$$

$$\mathbf{d}_{\text{total},y} = C_1 e^{i\omega t} + \tilde{C}_1 e^{-i\omega t}, \quad (20)$$

where,

$$B_1 = -\kappa A_{\text{sp}} E_0 V (\hat{a}_1^* + \hat{a}_{-1}^*) + f_{\mathbf{K}} d_0 + f_{\mathbf{K}'} d_0, \quad (21)$$

$$C_1 = i\kappa A_{\text{sp}} E_0 V (\hat{a}_1^* - \hat{a}_{-1}^*) + i f_{\mathbf{K}} d_0 - i f_{\mathbf{K}'} d_0, \quad (22)$$

$$\kappa = \frac{\text{Re}[\epsilon_{\text{metal}} - \epsilon_d]}{4\pi} \quad (23)$$

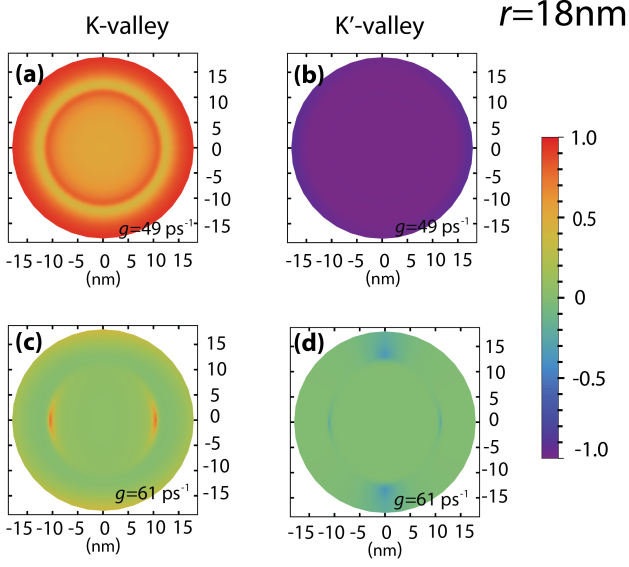


FIG. 5. Inversion population of K and K' valleys of MoS_2 nanoflake with the radius of 18 nm. The gain is (a),(b) 49 ps^{-1} and (c),(d) 61 ps^{-1} . The panels (a), (c) correspond to the K valley, while the panels (b), (d) describe the K' valley.

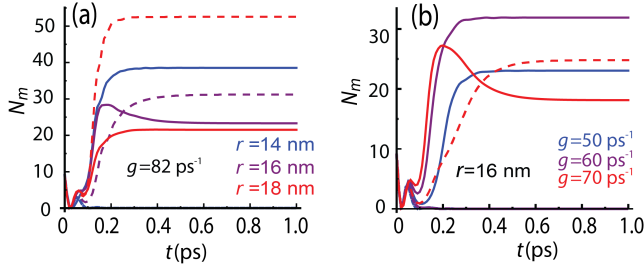


FIG. 6. The number of surface plasmons, N_m , as a function of time t for topological spaser with MoS_2 nanoflake as a gain medium. The solid and dashed lines correspond to $m = 1$ and $m = -1$ plasmons, respectively. The initial number of plasmons is $N_1 = N_{-1} = 9$. (a) The gain is $g = 82 \text{ ps}^{-1}$ and the radii of TMDC nanoflake are 14 nm, 16 nm, and 18 nm. The corresponding lines are shown by different colors as marked in the panel. (b) The radius of TMDC nanoflake is 16 nm and the gain is 50 ps^{-1} , 60 ps^{-1} , and 70 ps^{-1} . The corresponding lines are shown by different colors as marked in the panel.

$$\mathbf{f}_{\mathbf{K}} = -\nu \sum_{\mathbf{S}} \frac{i n_{\mathbf{K}}(\mathbf{r}) \sum_{m=1,-1} \tilde{\Omega}_{m,\mathbf{K}}^* a_m^*}{-(\omega - \Delta_g) + i\Gamma_{12}}, \quad (24)$$

$$\mathbf{f}_{\mathbf{K}'} = -\nu \sum_{\mathbf{S}} \frac{i n_{\mathbf{K}'}(\mathbf{r}) \sum_{m=1,-1} \tilde{\Omega}_{m,\mathbf{K}'}^* a_m^*}{-(\omega - \Delta_g) + i\Gamma_{12}}, \quad (25)$$

$$\mathbf{d}_{\mathbf{K}} = d_0 \mathbf{e}_+ \quad \& \quad \mathbf{d}_{\mathbf{K}'} = d_0 \mathbf{e}_-. \quad (26)$$

The derivation of Eqs. (21)- (25) is given in the Supporting Materials. The main contribution to the total dipole moment comes from the metal nanospheroid, for

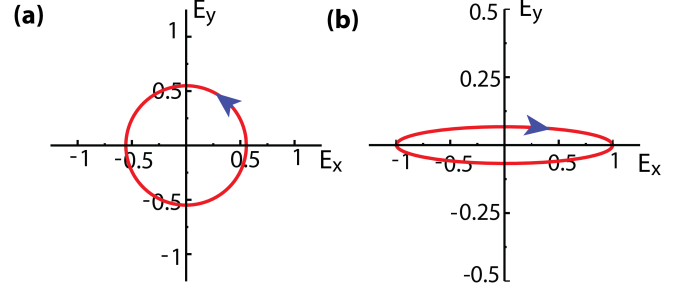


FIG. 7. Polarization ellipse of the far field radiation of topological spaser for its two regimes of continuous wave operation. (a) Radius of TMDC nanoflake is 16 nm and the gain is 49 ps^{-1} . Only $m = 1$ plasmon mode is generated. The far field radiation is left circularly polarized. (b) Radius of TMDC nanoflake is 16 nm and the gain is 70 ps^{-1} . Two plasmon modes, $m = 1$ and $m = -1$ are generated. The far field radiation is right elliptically polarized. The electric field is shown in arbitrary units.

which the corresponding dipole moment is almost two order of magnitude larger than the dipole moment of TMDC nanoflake.

The components of the dipole radiated field are proportional to the total dipole moment, $E_x \propto \mathbf{d}_{\text{total},x}$, $E_y \propto \mathbf{d}_{\text{total},y}$. The corresponding polarization ellipse is shown in Fig. 7 for two regimes of operation of the topological spaser: (a) only one $m = 1$ plasmon mode is generated and (b) two modes, $m = 1$ and $m = -1$, are cogenerated. For case (a), the far field radiation is left circularly polarized, which is the same polarization as the one of the pump light. This is consistent with the condition that only one plasmon mode is generated in this case.

If two plasmon modes are generated [Fig. 7(b)], then the corresponding polarization ellipse describes the right elliptically polarized radiation. Note, that the pump light is left circularly polarized. The change of the handedness of polarization from left to right is due to the fact that the number of $m = -1$ plasmons is greater than the number of $m = 1$ plasmons in the continuous wave regime of the spaser.

Thus, for a given radius of TMDC nanoflake, by changing the gain, i.e., the intensity of the circularly polarized light, we can switch the handedness of the far field radiation from left to right and vice versa. For example, if $g_{th1} < g < g_{th2}$ then the far field radiation is left circularly polarized, but if $g_{th2} < g$ then it is right elliptically polarized.

IV. CONCLUSION

A topological nanospaser of type II consists of two main components: a metal nanospheroid and a TMDC, e.g., MoS_2 , monolayer flake of a circular shape. The

nanospheroid functions as a plasmonic nanoresonator with two relevant plasmonic modes, which rotate in the opposite directions and are characterized by azimuthal quantum numbers $m = \pm 1$. The MoS₂ monolayer is a gain medium with nontrivial topology. It is placed atop of a nanospheroid and has two chiral *valleys*, K and K' . The system is pumped by a circular polarized light, which populates the conduction band states of only one valley, say the K valley.

Such topological spaser has been theoretically proposed in Ref. [15]. In the present paper we show that it has very rich dynamics, which strongly depends on the radius of the gain medium (TMDC nanoflake). If the radius of TMDC is small, then the K and K' valleys are mainly coupled to the co-rotating plasmonic modes, e.g., the K valley is coupled to the $m = 1$ mode. In this case the nanospaser has one threshold, g_{th} , so that if the gain is larger than g_{th} then the co-rotating plasmon mode is generated. For larger radius of nanoflake, the valleys of TMDC become also strongly coupled to the counter-rotating modes, and the nanospaser has two thresholds, $g_{th,1}$ and $g_{th,2}$, so that if $g_{th,2} > g > g_{th,1}$ then only the co-rotating mode is generated, while if $g > g_{th,2}$ then both co-rotating and counter-rotating modes are generated. For even larger radius of TMDC, the two thresholds merge into one and the nanospaser has only one regime when two modes, $m = 1$ and $m = -1$, are cogenerated. In this case the number of counter-rotating plasmons is larger than the number of co-rotating ones. Because of that property the far-field radiation of nanospaser shows interesting behavior. Namely, by changing the gain strength, one can change the handedness of the far-field radiation from left to right and vice versa.

All these unique properties of topological nanospaser make it an extremely viable option for several nanoscopic applications. Main areas are near-field spectroscopy and sensing where a plasmon frequency of a nanospaser can be tuned to work at the required condition. However, the topological nanospaser can also be used in optical interconnects and probing. Another key area is the biomedical one where similar systems have been previously adopted [11, 14] for the diagnosis and therapeutics of cancer. With added topological chiral benefits, this nanolaser can be more effective in such detection. In addition to all these, the topological nanospaser has also a potential as an excellent far-field radiation source.

V. ACKNOWLEDGMENT

Major funding was provided by Grant No. DE-SC0007043 from the Materials Sciences and Engineering Division of the Office of the Basic Energy Sciences, Office of Science, U.S. Department of Energy. Numerical simulations have been performed using support by Grant No. DE-FG02-01ER15213 from the Chemical Sciences, Biosciences and Geosciences Division, Office of Basic Energy Sciences, Office of Science, US Department of Energy.

VI. SUPPORTING INFORMATION

A. Metallic Oblate Spheroid: Geometry and Modes

We consider an oblate spheroid, which in the Cartesian coordinate system is described by the following equation

$$\frac{x^2 + y^2}{a^2} + \frac{z^2}{c^2} = 1, \quad (27)$$

where a and c are semi-axes, $\varepsilon = \sqrt{1 - \frac{c^2}{a^2}}$ is the eccentricity of the spheroid.

It is convenient to introduce the spheroidal coordinates, ξ , η and φ , which are related to the Cartesian coordinates, x , y and z through the following expression [43]:

$$x = f\sqrt{\xi^2 + 1}\sqrt{1 - \eta^2} \cos(\varphi), \quad (28)$$

$$y = f\sqrt{\xi^2 + 1}\sqrt{1 - \eta^2} \sin(\varphi), \quad (29)$$

$$z = f\xi\eta, \quad (30)$$

where $0 \leq \xi < \infty$, $-1 \leq \eta \leq 1$, $0 \leq \varphi < 2\pi$ and $f = \varepsilon a$.

Then the surface plasmon eigenmodes of the metal spheroid are described by the quasistatic equation [37]

$$\nabla[\theta(\mathbf{r})\nabla\phi_m] = s_{sp}\nabla^2\phi_m, \quad (31)$$

where s_{sp} is the eigenvalue of the corresponding mode ϕ_m . Here $\theta(\mathbf{r})$ is the characteristic function that is 1 inside the metal and 0 elsewhere. For oblate spheroid, the eigenmodes are characterized by multipole quantum number l and magnetic quantum number m . For the relevant modes of topological nanospaser, the multipole quantum number is 1, $l = 1$. Then the corresponding eigenmodes are described by the following expressions

$$\phi_m = C_N P_1^m(\eta) e^{im\varphi} \begin{cases} \frac{P_1^m(i\xi)}{P_1^m(i\xi_0)}, & 0 < \xi < \xi_0, \\ \frac{Q_1^m(i\xi)}{Q_1^m(i\xi_0)}, & \xi_0 < \xi, \end{cases} \quad (32)$$

where $P_l^m(x)$ and $Q_l^m(x)$ are the Legendre functions of the first and second kind, respectively, and $\xi_0 = \frac{\sqrt{1-\varepsilon^2}}{\varepsilon}$. The constant C_N is determined by normalization condition,

$$\int_{\text{All Space}} |\nabla\phi(\mathbf{r})_m|^2 d^3\mathbf{r} = 1. \quad (33)$$

Due to axial symmetry of the nanospheroid, the corresponding eigenvalues, s_{sp} , do not depend on m . They can be also found from the following expression [3, 36]

$$s_{sp} = \frac{\int_{\text{All Space}} \theta(\mathbf{r}) |\nabla\phi_m(\mathbf{r})|^2 d^3\mathbf{r}}{\int_{\text{All Space}} |\nabla\phi_m(\mathbf{r})|^2 d^3\mathbf{r}}. \quad (34)$$

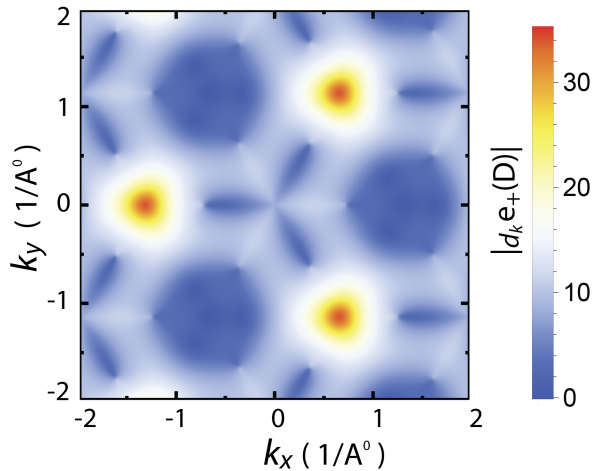


FIG. 8. Absolute value of the left-rotating chiral dipole component, $\mathbf{d}_- = \mathbf{e}_+ \mathbf{d}$, in MoS₂

Using explicit expression (32) for ϕ_m , we derive the final equation for the eigenvalue

$$s_{\text{sp}} = \frac{\frac{dP_1^m(x)}{dx}}{\frac{dP_1^m(x)}{dx} - \frac{P_1^m(x)}{Q_1^m(x)} \frac{dQ_1^m(x)}{dx}} \Bigg|_{x=i\xi_0}. \quad (35)$$

To find the plasmon frequency, ω_{sp} , and the plasmon relaxation rate, γ_{sp} , we use the following relations [3, 36]:

$$s_{\text{sp}} = \text{Re}[s(\omega_{\text{sp}})], \quad (36)$$

$$r_{\text{sp}} = \frac{\text{Im}[s(\omega_{\text{sp}})]}{s'_{\text{sp}}}, \quad s'_{\text{sp}} \equiv \frac{d\text{Re}[s(\omega)]}{d\omega} \Bigg|_{\omega=\omega_{\text{sp}}}, \quad (37)$$

where the Bergman spectral parameter is defined as

$$s(\omega) = \frac{\epsilon_d}{\epsilon_d - \epsilon_m(\omega)}. \quad (38)$$

Here ϵ_d is the dielectric constant of surrounding medium, and $\epsilon_m(\omega)$ is the dielectric function of the metal (silver). In our computations, for silver, we use the dielectric function from Ref. [17].

B. TMDC Parameters

In our calculations the TMDC (MoS₂) monolayer is characterized by its bandgap and the dipole matrix elements between the conduction and valence bands at the K and K' points. To find these parameters we have used a three-band tight binding model [21]. The calculated values of the transition dipole matrix elements and the bandgap are given in Table I. The dipole matrix elements at the K and K' points are purely chiral. They are proportional to $\mathbf{e}_{\pm} = 2^{-1/2}(\mathbf{e}_x \pm i\mathbf{e}_y)$, where \mathbf{e}_x and \mathbf{e}_y are the Cartesian unit vectors. The plot of the absolute value of the chiral dipole, $|\mathbf{d}_{\pm}|$, where $\mathbf{d}_{\pm} = \mathbf{e}_{\pm}^* \mathbf{d}$, is shown in Fig. 8.

TMDC	Semi-principal axis c (nm)	Dipole elements (D)		Band gap (eV)
		\mathbf{d}_K	$\mathbf{d}_{K'}$	
MoS ₂	1.20	17.68 \mathbf{e}_+	17.68 \mathbf{e}_-	1.66
MoSe ₂	1.45	19.23 \mathbf{e}_+	19.23 \mathbf{e}_-	1.79
WSe ₂	0.85	18.38 \mathbf{e}_+	18.38 \mathbf{e}_-	1.43
MoTe ₂	1	20.08 \mathbf{e}_+	20.08 \mathbf{e}_-	1.53

TABLE I. Parameters employed in the calculations: Semi-principal axes of the spheroids, and the dipole matrix elements and band gaps of the TMDCs.

C. Far-field radiation

The total dipole moment of the spaser can be expressed in the following form

$$\mathbf{d}_{\text{total}} = \mathbf{d}_{\text{metal}} + \mathbf{d}_{\text{tmcdc}}, \quad (39)$$

where $\mathbf{d}_{\text{metal}}$ is the dipole moment of the metal nanospheroid and $\mathbf{d}_{\text{tmcdc}}$ is the dipole moment of the TMDC nanoflake.

1. Dipole moment of the metal nanospheroid

The electric field inside the metal, which is produced by generated plasmon modes, both $m = 1$ and $m = -1$, is uniform and is given by the following expression

$$\mathbf{F}_m(\mathbf{r}, t) = - \sum_{m=1,-1} A_{\text{sp}} (\nabla \phi_m \hat{a}_m e^{-i\omega t} + \nabla \phi_m^* \hat{a}_m^* e^{i\omega t}), \quad (40)$$

where

$$A_{\text{sp}} = \sqrt{\frac{4\pi \hbar s(\omega)}{\epsilon_d s'(\omega)}} \quad (41)$$

and

$$s(\omega) = \frac{\epsilon_d}{\epsilon_d - \epsilon_m(\omega)}, \quad (42)$$

Then the dipole moment of the metal nanospheroid can be found from the following expression

$$\mathbf{d}_{\text{metal}} = \int_V \mu \mathbf{F}_m(\mathbf{r}, t) dv \quad (43)$$

where

$$\mu = \frac{\text{Re}[\epsilon_{\text{metal}} - \epsilon_d]}{4\pi}. \quad (44)$$

Taking into account that the electric field inside the metal is a constant, $E_0 = |\nabla \phi_m|$, we derive the following expressions for the dipole moment of the metal

nanospheroid

$$\mathbf{d}_{\text{metal},\mathbf{x}} = -\mu A_{\text{sp}} E_0 V \left((\hat{a}_1 e^{-i\omega t} + \hat{a}_1^* e^{i\omega t}) + (\hat{a}_{-1} e^{-i\omega t} + \hat{a}_{-1}^* e^{i\omega t}) \right) \quad (45)$$

$$\mathbf{d}_{\text{metal},\mathbf{y}} = -\mu A_{\text{sp}} E_0 V \left(i(\hat{a}_1 e^{-i\omega t} - \hat{a}_1^* e^{i\omega t}) - i(\hat{a}_{-1} e^{-i\omega t} - \hat{a}_{-1}^* e^{i\omega t}) \right) \quad (46)$$

2. Dipole moment of TMDC monolayer

The density matrix of TMDC nanoflake has the following structure

$$\hat{\rho}_{\mathcal{K}}(\mathbf{r}, t) = \begin{pmatrix} \rho_{\mathcal{K}}^{(c)}(\mathbf{r}, t) & \rho_{\mathcal{K}}(\mathbf{r}, t) e^{i\omega t} \\ \rho_{\mathcal{K}}^*(\mathbf{r}, t) e^{-i\omega t} & \rho_{\mathcal{K}}^{(v)}(\mathbf{r}, t) \end{pmatrix}. \quad (47)$$

where \mathcal{K} is the valley index, K or K' . The off-diagonal elements, i.e., coherences, determine the dipole moment of TMDC system

$$\mathbf{d}_{\text{tmDC}} = \sum_{\mathbf{S}} \sum_{\mathcal{K}=\mathbf{K},\mathbf{K}'} (\rho_{\mathcal{K}}(\mathbf{r}) \mathbf{d}_{\mathcal{K}} e^{i\omega t} + \rho_{\mathcal{K}}^*(\mathbf{r}) \mathbf{d}_{\mathcal{K}}^* e^{-i\omega t}) + h.c., \quad (48)$$

where $\sum_{\mathbf{S}}$ is the sum (integral) over all points \mathbf{r} of TMDC nanoflake.

The coherences satisfy the following stationary equation (see Eq. (12) of the main text)

$$[-i(\omega - \omega_{21}) - \Gamma_{12}] \rho_{\mathcal{K}}(\mathbf{r}) + in_{\mathcal{K}}(\mathbf{r}) \sum_{m=1,-1} \tilde{\Omega}_{m,\mathcal{K}}^*(\mathbf{r}) a_m^* = 0, \quad (49)$$

where Γ_{12} is the polarization relaxation rate, $n_{\mathcal{K}}$ is the population inversion defined as

$$n_{\mathcal{K}} \equiv \rho_{\mathcal{K}}^{(c)} - \rho_{\mathcal{K}}^{(v)}, \quad (50)$$

and

$$\tilde{\Omega}_{m,\mathcal{K}}(\mathbf{r}) = -\frac{1}{\hbar} A_{\text{sp}} \nabla \phi_m(\mathbf{r}) \mathbf{d}_{\mathcal{K}}. \quad (51)$$

From Eq. (49) we can find the stationary coherences of TMDC monolayer

$$\rho_{\mathcal{K}}(\mathbf{r}) = -\frac{in_{\mathcal{K}}(\mathbf{r}) \sum_{m=1,-1} \tilde{\Omega}_{m,\mathcal{K}}^*(\mathbf{r}) a_m^*}{-(\omega - \omega_{21}) + i\Gamma_{12}}. \quad (52)$$

We substitute Eq. (52) into Eq. (48) and obtain the following expression for the dipole moment of TMDC

$$\mathbf{d}_{\text{tmDC}} = \mathbf{f}_{\mathbf{K}} \mathbf{d}_{\mathbf{K}} e^{i\omega t} + \mathbf{f}_{\mathbf{K}'} \mathbf{d}_{\mathbf{K}'} e^{i\omega t} + h.c., \quad (53)$$

where the following notations were introduced

$$\mathbf{f}_{\mathbf{K}} = -\nu \sum_{\mathbf{S}} \frac{in_{\mathbf{K}}(\mathbf{r}) \sum_{m=1,-1} \tilde{\Omega}_{m,\mathbf{K}}^* a_m^*}{-(\omega - \Delta_g) + i\Gamma_{12}} \quad (54)$$

$$\mathbf{f}_{\mathbf{K}'} = -\nu \sum_{\mathbf{S}} \frac{in_{\mathbf{K}'}(\mathbf{r}) \sum_{m=1,-1} \tilde{\Omega}_{m,\mathbf{K}'}^* a_m^*}{-(\omega - \Delta_g) + i\Gamma_{12}}. \quad (55)$$

Taking into account that $\mathbf{d}_{\mathbf{K}} = d_0(1, i)$ and $\mathbf{d}_{\mathbf{K}'} = d_0(1, -i)$ we obtain the x and y components of the dipole moment

$$\mathbf{d}_{\text{tmDC},\mathbf{x}} = \mathbf{f}_{\mathbf{K}} d_0 e^{i\omega t} + \mathbf{f}_{\mathbf{K}'} d_0 e^{i\omega t} + h.c. \quad (56)$$

$$\mathbf{d}_{\text{tmDC},\mathbf{y}} = i\mathbf{f}_{\mathbf{K}} d_0 e^{i\omega t} - i\mathbf{f}_{\mathbf{K}'} d_0 e^{i\omega t} + h.c. \quad (57)$$

3. Far field dipole radiation

The total dipole moment of the spaser system is the sum of the dipole moment of the metal nanospheroid and TMDC nanoflake. Its x and y components can be expressed as

$$\mathbf{d}_{\text{total},\mathbf{x}} = -\mu A_{\text{sp}} E_0 V (\hat{a}_1 e^{-i\omega t} + \hat{a}_{-1} e^{-i\omega t} + h.c.) + (\mathbf{f}_{\mathbf{K}} d_0 e^{i\omega t} + \mathbf{f}_{\mathbf{K}'} d_0 e^{i\omega t} + h.c.) \quad (58)$$

$$\mathbf{d}_{\text{total},\mathbf{y}} = -\mu A_{\text{sp}} E_0 V (i\hat{a}_1 e^{-i\omega t} - i\hat{a}_{-1} e^{-i\omega t} + h.c.) + (i\mathbf{f}_{\mathbf{K}} d_0 e^{i\omega t} - i\mathbf{f}_{\mathbf{K}'} d_0 e^{i\omega t} + h.c.) \quad (59)$$

These expressions have the following structure

$$\mathbf{d}_{\text{total},\mathbf{x}} = 2\text{Re} [B_x e^{i\omega t}], \quad (60)$$

$$\mathbf{d}_{\text{total},\mathbf{y}} = 2\text{Re} [B_y e^{i\omega t}], \quad (61)$$

where,

$$B_x = -\mu A_{\text{sp}} E_0 V (\hat{a}_1^* + \hat{a}_{-1}^*) + \mathbf{f}_{\mathbf{K}} d_0 + \mathbf{f}_{\mathbf{K}'} d_0, \quad (62)$$

$$B_y = i\mu A_{\text{sp}} E_0 V (\hat{a}_1^* - \hat{a}_{-1}^*) + i\mathbf{f}_{\mathbf{K}} d_0 - i\mathbf{f}_{\mathbf{K}'} d_0. \quad (63)$$

The total dipole moment of the system determines the far-field radiation of the spaser. The polarization of radiation is characterized by the x and y components of the far electric field, which are proportional to the corresponding components of the dipole moment, i.e., $\mathbf{d}_{\text{total},\mathbf{x}}$ and $\mathbf{d}_{\text{total},\mathbf{y}}$, while the total radiation power is given by the following expression

$$\begin{aligned} I &= \frac{4}{3} \left(\frac{\omega}{c_0} \right)^3 \frac{(\epsilon_d)^{1/2}}{\hbar} \langle |\mathbf{d}_{\text{total}}|^2 \rangle \\ &= \frac{8}{3} \left(\frac{\omega}{c_0} \right)^3 \frac{(\epsilon_d)^{1/2}}{\hbar} (|B_x|^2 + |B_y|^2) \end{aligned} \quad (64)$$

where $\langle \dots \rangle$ means the time average.

-
- [1] G. S. Agarwal. Rotating-wave approximation and spontaneous emission. *Phys. Rev. A*, 4:1778–1781, Nov 1971.
- [2] D. G. Baranov, A. P. Vinogradov, A. A. Lisyansky, Y. M. Strel'niker, and D. J. Bergman. Magneto-optical spaser. *Opt. Lett.*, 38:2002–2004, 2013.
- [3] D. J. Bergman and M. I. Stockman. Surface plasmon amplification by stimulated emission of radiation: Quantum generation of coherent surface plasmons in nanosystems. *Phys. Rev. Lett.*, 90:027402–1–4, 2003.
- [4] F. Bloch and A. Siegert. Magnetic resonance for nonrotating fields. *Phys. Rev.*, 57:522–527, Mar 1940.
- [5] T. Cao, G. Wang, W. Han, H. Ye, C. Zhu, J. Shi, Q. Niu, P. Tan, E. Wang, B. Liu, and J. Feng. Valley-selective circular dichroism of monolayer molybdenum disulfide. *Nat. Commun.*, 3:887–1–5, 2012.
- [6] Pi-Ju Cheng, Zhen-Ting Huang, Jhu-Hong Li, Bo-Tsun Chou, Yu-Hsun Chou, Wei-Cheng Lo, Kuo-Ping Chen, Tien-Chang Lu, and Tzy-Rong Lin. High-performance plasmonic nanolasers with a nanotrench defect cavity for sensing applications. 5(7):2638–2644, 2018.
- [7] B. T. Chou, Y. H. Chou, Y. M. Wu, Y. C. Chung, W. J. Hsueh, S. W. Lin, T. C. Lu, T. R. Lin, and S. D. Lin. Single-crystalline aluminum film for ultraviolet plasmonic nanolasers. *Sci. Rep.*, 6:19887–1–9, 2016.
- [8] K Ding, JO Diaz, D Bimberg, Cun-Zheng Modulation bandwidth and energy efficiency of metallic cavity semiconductor nanolasers with inclusion of noise effects. 9(5):488–497, 2015.
- [9] K Ding, Cun-Zheng Metallic subwavelength-cavity semiconductor nanolasers. 1(7):e20–e20, 2012.
- [10] V Dolores-Calzadilla, B Romeira, F Pagliano, S Birindelli, A Higuera-Rodriguez, PJ Van Veldhoven, MK Smit, A Fiore, and D Waveguide-coupled nanopillar metal-cavity light-emitting diodes on silicon. 8(1):1–8, 2017.
- [11] Xudong Fan and Seok-Hyun The potential of optofluidic biolasers. 11(2):141–147, 2014.
- [12] D. Y. Fedyanin. Toward an electrically pumped spaser. *Opt. Lett.*, 37:404–406, 2012.
- [13] R. A. Flynn, C. S. Kim, I. Vurgaftman, M. Kim, J. R. Meyer, A. J. Mäkinen, K. Bussmann, L. Cheng, F. S. Choa, and J. P. Long. A room-temperature semiconductor spaser operating near 1.5 micron. *Opt. Express*, 19:8954–8961, 2011.
- [14] E. I. Galanzha, R. Weingold, D. A. Nedosekin, M. Sarimollaoglu, J. Nolan, W. Harrington, A. S. Kuchyanov, R. G. Parkhomenko, F. Watanabe, Z. Nima, A. S. Biris, A. I. Plekhanov, M. I. Stockman, and V. P. Zharov. Spaser as a biological probe. *Nat. Commun.*, 8:15528–1–7, 2017.
- [15] Rupesh Ghimire, Jhih-Sheng Wu, Vadym Apalkov, and Mark I Stockman. Topological nanospaser. 1(advance-print), 2020.
- [16] Y.-W. Huang, W. T. Chen, P. C. Wu, V. A. Fedotov, N. I. Zheludev, and D. P. Tsai. Toroidal lasing spaser. *Sci. Rep.*, 3:1237–1–4, 2013.
- [17] P. B. Johnson and R. W. Christy. Optical constants of noble metals. *Phys. Rev. B*, 6:4370–4379, 1972.
- [18] M Khajavikhan, A Simic, M Katz, JH Lee, B Slutsky, A Mizrahi, V Lomakin, and Y Thresholdless nanoscale coaxial lasers. 482(7384):204–207, 2012.
- [19] C.-J. Lee, H. Yeh, F. Cheng, P.-H. Su, T.-H. Her, Y.-C. Chen, C.-Y. Wang, S. Gwo, S. R. Bank, C.-K. Shih, and W.-H. Chang. Low-threshold plasmonic lasers on a single-crystalline epitaxial silver platform at telecom wavelength. *ACS Photonics*, 4:1431–1439, 2017.
- [20] K. Li, X. Li, M. I. Stockman, and D. J. Bergman. Surface plasmon amplification by stimulated emission in nanolenses. *Phys. Rev. B*, 71:115409–1–4, 2005.
- [21] G. B. Liu, W. Y. Shan, Y. G. Yao, W. Yao, and D. Xiao. Three-band tight-binding model for monolayers of group-VIB transition metal dichalcogenides. *Phys. Rev. B*, 88:085433–1–10, 2013.
- [22] Y.-J. Lu, C.-Y. Wang, J. Kim, H.-Y. Chen, M.-Y. Lu, Y.-C. Chen, W.-H. Chang, L.-J. Chen, M. I. Stockman, C.-K. Shih, and S. Gwo. All-color plasmonic nanolasers with ultralow thresholds: Autotuning mechanism for single-mode lasing. *Nano Lett.*, 14:4381–4388, 2014.
- [23] R. Ma, X. Yin, R. F. Oulton, V. J. Sorger, and X. Zhang. Multiplexed and electrically modulated plasmon laser circuit. *Nano Lett.*, page doi: 10.1021/nl302809a, 2012.
- [24] R.-M. Ma, S. Ota, Y. Li, S. Yang, and X. Zhang. Explosives detection in a lasing plasmon nanocavity. *Nature Nanotechnology*, 9:600–604, 2014.
- [25] R.-M. Ma, R. F. Oulton, V. J. Sorger, G. Bartal, and X. Zhang. Room-temperature sub-diffraction-limited plasmon laser by total internal reflection. *Nat. Mater.*, 10:110–113, 2010.
- [26] M. J. H. Marel, B. Smalbrugge, E. J. Geluk, P. J. van Veldhoven, B. Barcones, B. Koopmans, R. Nötzel, M. K. Smit, and M. T. Hill. Plasmonic distributed feedback lasers at telecommunications wavelengths. *Opt. Express*, 19:15109–15118, 2011.
- [27] Fatemeh Nematollahi, S. Azar Oliaei Motlagh, Jhih-Sheng Wu, Rupesh Ghimire, Vadym Apalkov, and Mark I. Stockman. Topological resonance in weyl semimetals in a circularly polarized optical pulse. *Phys. Rev. B*, 102:125413, Sep 2020.
- [28] Cun-Zheng Semiconductor nanolasers and the size-energy-efficiency challenge: a review. 1(1):014002, 2019.
- [29] M. A. Noginov, G. Zhu, A. M. Belgrave, R. Bakker, V. M. Shalaev, E. E. Narimanov, S. Stout, E. Herz, T. Suteewong, and U. Wiesner. Demonstration of a spaser-based nanolaser. *Nature*, 460:1110–1112, 2009.
- [30] R. F. Oulton, V. J. Sorger, T. Zentgraf, R.-M. Ma, C. Gladden, L. Dai, G. Bartal, and X. Zhang. Plasmon lasers at deep subwavelength scale. *Nature*, 461:629–632, 2009.
- [31] E. Plum, V. A. Fedotov, P. Kuo, D. P. Tsai, and N. I. Zheludev. Towards the lasing spaser: Controlling meta-material optical response with semiconductor quantum dots. *Opt. Express*, 17:8548–8551, 2009.
- [32] Omid Salehzadeh, Mehrdad Djavid, Nhung Hong Tran, Ishiang Shih, and Zetian Mi. Optically pumped two-dimensional mos2 lasers operating at room-temperature. *Nano letters*, 15(8):5302–5306, 2015.
- [33] Janelle Shane, Qing Gu, Felipe Vallini, Brett Wingad, Joseph ST Smalley, Newton C Frateschi, and Yeshiahu Fainman. Thermal considerations in electrically-pumped metallo-dielectric nanolasers. In *Physics and Simulation of Optoelectronic Devices XXII*, volume 8980, page 898027. International Society for Optics and Photonics.

- [34] Kun-Ching Shen, Chen-Ta Ku, Chiieh Hsieh, Hao-Chung Kuo, Yuh-Jen Cheng, and Din Ping Deep-ultraviolet hyperbolic metacavity laser. 30(21):1706918, 2018.
- [35] M. Stockman. Spasers to speed up cmos processors, 2018.
- [36] M. I. Stockman. The spaser as a nanoscale quantum generator and ultrafast amplifier. *Journal of Optics*, 12:024004–1–13, 2010.
- [37] M. I. Stockman, S. V. Faleev, and D. J. Bergman. Localization versus delocalization of surface plasmons in nanosystems: Can one state have both characteristics? *Phys. Rev. Lett.*, 87:167401–1–4, 2001.
- [38] S. Sun, C. Zhang, K. Wang, S. Wang, S. Xiao, and Q. Song. Lead halide perovskite nanoribbon based uniform nanolaser array on plasmonic grating. *ACS Photonics*, 4:649–656, 2017.
- [39] F. v. Beijnum, P. J. v. Veldhoven, E. J. Geluk, M. J. A. d. Dood, G. W. t. Hooft, and M. P. v. Exter. Surface plasmon lasing observed in metal hole arrays. *Phys. Rev. Lett.*, 110:206802–1–5, 2013.
- [40] S. Wang, B. Li, X. Y. Wang, H. Z. Chen, Y. L. Wang, X. W. Zhang, L. Dai, and R. M. Ma. High-yield plasmonic nanolasers with superior stability for sensing in aqueous solution. *ACS Photonics*, 4:1355–1360, 2017.
- [41] Suo Wang, Bo Li, Xing-Yuan Wang, Hua-Zhou Chen, Yi-Lun Wang, Xiao-Wei Zhang, Lun Dai, and Ren-Min High-yield plasmonic nanolasers with superior stability for sensing in aqueous solution. 4(6):1355–1360, 2017.
- [42] Xing-Yuan Wang, Yi-Lun Wang, Suo Wang, Bo Li, Xiao-Wei Zhang, Lun Dai, and Ren-Min Lasing enhanced surface plasmon resonance sensing. 6(2):472–478, 2017.
- [43] M. Willatzen and L. C. L. Y. Voon. Oblate spheroidal coordinates. In *Separable Boundary-Value Problems in Physics*, pages 155–164. Wiley-VCH, Weinheim, Germany, 2011.
- [44] Sajith Withanage, Tharanga Nanayakkara, U. Wijewardena, Annika Kriisa, and R. Mani. The role of surface morphology on nucleation density limitation during the cvd growth of graphene and the factors influencing graphene wrinkle formation. *Journal Name: MRS Advances; Journal Volume: 4; Journal Issue: 61-62*, page Medium: X; Size: 3337 to 3345, 2019.
- [45] Jhih-Sheng Wu, Vadym Apalkov, and Mark I. Stockman. Topological spaser. *arXiv: 1909.11113 [cond-mat.mes-hall]*, 2019.
- [46] Sanfeng Wu, Sonia Buckley, John R Schaibley, Liefeng Feng, Jiaqiang Yan, David G Mandrus, Fariba Hatami, Wang Yao, Jelena Vuckovic, and Arka Majumdar. Ultra-low threshold monolayer semiconductor nanocavity lasers. *arXiv preprint arXiv:1502.01973*, 2015.
- [47] Z. Wu, J. Chen, Y. Mi, X. Sui, S. Zhang, W. Du, R. Wang, J. Shi, X. Wu, X. Qiu, Z. Qin, Q. Zhang, and X. Liu. All-inorganic cspbbr₃ nanowire based plasmonic lasers. *Advanced Optical Materials*, pages 1800674–1–8, 2018.
- [48] Z. Ye, D. Sun, and T. F. Heinz. Optical manipulation of valley pseudospin. *Nat. Phys.*, 13:26–30, 2016.
- [49] Q. Zhang, G. Li, X. Liu, F. Qian, Y. Li, T. C. Sum, C. M. Lieber, and Q. Xiong. A room temperature low-threshold ultraviolet plasmonic nanolaser. *Nat. Commun.*, 5:4953–1–9, 2014.
- [50] N. I. Zheludev, S. L. Prosvirnin, N. Papisimakis, and V. A. Fedotov. Lasing spaser. *Nat. Phot.*, 2:351–354, 2008.
- [51] W. Zhou, M. Dridi, J. Y. Suh, C. H. Kim, D. T. Co, M. R. Wasielewski, G. C. Schatz, and T. W. Odom. Lasing action in strongly coupled plasmonic nanocavity arrays. *Nature Nano*, 8:506–511, 2013.
- [52] Wenqi Zhu, Ting Xu, Haozhu Wang, Cheng Zhang, Parag B Deotare, Amit Agrawal, and Henri J Surface plasmon polariton laser based on a metallic trench fabry-perot resonator. 3(10):e1700909, 2017.